Spatial Angular Compounding of Photoacoustic Images

Hyun Jae Kang, Muyinatu A Lediju Bell*, Xiaoyu Guo, and Emad M. Boctor

***Abstract*—Photoacoustic (PA) images utilize pulsed lasers and ultrasound transducers to visualize targets with higher optical absorption than the surrounding medium. However, they are susceptible to acoustic clutter and background noise artifacts that obfuscate biomedical structures of interest. We investigated three spatial-angular compounding methods to improve PA image quality for biomedical applications, implemented by combining multiple images acquired as an ultrasound probe was rotated about the elevational axis with the laser beam and target fixed. Compounding with conventional averaging was based on the pose information of each PA image, while compounding with weighted and selective averaging utilized both the pose and image content information. Weighted-average compounding enhanced PA images with the least distortion of signal size, particularly when there were large (i.e., 2.5 mm and 7°) perturbations from the initial probe position. Selective-average compounding offered the best improvement in image quality with up 181, 1665, and 1568 times higher contrast, CNR, and SNR, respectively, compared to the mean values of individual PA images. The three presented spatial compounding methods have promising potential to enhance image quality in multiple photoacoustic applications.**

***Index Terms*—Biomedical imaging, biomedical image processing, ultrasonic imaging, image reconstruction, image enhancement.**

I. Introduction

PHOTOACOUSTIC (PA) imaging has achieved expansive growth in potential biomedical applications, clinical utility, and equipment configurations within the past decade. It is based on the photoacoustic effect, excited through localized light transmission, absorption, thermal expansion, and a resulting pressure transient whose amplitude relies on the optical, thermal, and mechanical properties of the target material [1]–[3]. The resulting photoacoustic image represents optical absorption differences in the target region and has potential to detect breast cancer [4], identify atherosclerotic plaques [5], monitor thermal therapy [6], and localize medical implants such as brachytherapy seeds [7]–[9]. However, similar to ultrasound (US) imaging [10]–[12], PA images suffer from noise artifacts such as acoustic clutter or reverberation that reduce image quality—e.g., contrast, signal-to-noise ratio (SNR), and contrast-to-noise ratio (CNR) [13]–[15]. In addition, PA images have poor contrast, SNR and CNR when a low-energy laser source such as a laser diode is used to generate the photoacoustic effect [16], [17].

Signal averaging is commonly used to improve the SNR of PA images when the ultrasound transducer, light source, and target are fixed in the same position [13], [16], [18]. However, this type of averaging reduces frame rates for real-time imaging applications and has limited ability to reduce statistically dependent background noise [19], [20]. In addition, this approach may not be suitable for the clinical environment when the ultrasound probe is hand-held as subtle motions are difficult to avoid. Thus, averaging multiple PA images from different hand-held scans without motion compensation degrades the temporal and spatial resolution of images [21].

To overcome the limitations of frame averaging, advanced methods that parallel advances in US have been investigated. Adaptive photoacoustic beamforming methods, similar to adaptive US beamforming [22], was investigated to improve the lateral resolution and quality of PA images [23]. However, they suffer from suboptimal performance when the SNR is low [24] and unusual artifacts caused by the non-linear and data-dependent processing methods. In addition, motion-based approaches were implemented to reduce artifacts in PA [15], [25] and US images [26] requiring deformation of the target relative the probe, which is not always feasible. Unlike previous methods which rely on signal amplitudes, the short-lag spatial coherence (SLSC) beamformer, which was originally developed for US images [27], [28], creates images based on spatial coherence, and it triples the effective penetration depth in photoacoustic images with no frame averaging required [14], [17], [29]. It may also be weighted by amplitude-based images to reduce clutter and provide spectroscopic information [30]. Yet, SLSC does not sufficiently reduce coherent noise artifacts [9], [31]. As an alternative to these advanced methods, Pan *et al.* [32] and Mitcham *et al.* [33] enhanced the contrast of PA images by altering implanted targets to increase optical

Manuscript received December 01, 2015; revised February 05, 2016; accepted February 11, 2016. Date of publication February 18, 2016; date of current version July 29, 2016. Financial support was provided by Johns Hopkins University internal funds, NIH grant R21-EB015638, and NSF grant IIS-1162095. M. A. Lediju Bell additionally acknowledges support from NIH grant K99-EB018994, the Ford Foundation, and the UNCF-Merck Science Initiative. *Asterisk indicates corresponding author.*

H. J. Kang is with the Department of Computer Science, Johns Hopkins University, Baltimore, MD 21218 USA.

*M. A. L. Bell is with the Department of Computer Science, Johns Hopkins University, Baltimore, MD 21218 USA.

X. Guo is with the Department of Electrical and Computer Engineering, Johns Hopkins University, Baltimore, MD 21218 USA.

E. M. Boctor is with the Department of Computer Science, Johns Hopkins University, Baltimore, MD 21218 USA, and with the Department of Electrical and Computer Engineering, Johns Hopkins University, Baltimore, MD 21218 USA, and also with the Department of Radiology, Johns Hopkins University, Baltimore, MD 21218 USA.

Color versions of one or more of the figures in this paper are available online at http://ieeexplore.ieee.org.

Digital Object Identifier 10.1109/TMI.2016.2531109

absorption, but this approach is not suitable for non-invasive clinical applications.

Spatial-angular compounding of PA images may be implemented with free hand motion to overcome many of the stated limitations with existing clutter reduction approaches by reducing noise artifacts that vary with different scan directions. The concept is similar to spatial compounding methods for improving the quality of US B-mode [10], [34]–[36], quantitative US [37], [38] and US strain [11], [39], [40] images. The success of spatial compounding of US images relies on the combination of fully decorrelated speckle patterns, which may be achieved with large relative translations [10] or rotations [41], deformation [26], or variations in transmit parameters, such as frequency [42] and beem steering [43]. Images containing any one of these variations are then registered and summed to create a compounded image.

We previously demonstrated that a free-hand approach to spatial compounding of PA images, when compared to conventional averaging of these images, enables the inclusion of images acquired with large spatial and angular deviations from an initial image with better preservation of the signal resolution [21]. To implement the technique, an external spatial tracking device such as an electromagnetic (EM) position sensor is used to simultaneously record the spatial position and orientation (i.e., pose) information of the ultrasound probe and acquire PA images [44]. This pose information is used to filter images in similar planes, and the filtered images are combined with user-defined thresholds to form a single compounded PA image.

In this paper, we propose novel compounding methods that automatically select images for spatial registration and rely on image content information to reduce tracking error. We compare the image quality of these compounded PA images with a more coventional compounding method and discuss possible clinical applications. The specialized hardware and software integration of multiple system components required to achieve this novel imaging task is also described. To the authors' knowledge, this is the first study to present spatial angular compounding of photoacoustic images for improved image quality and integrate this approach with spatial tracking of photoacoustic images acquired with a handheld probe.

II. Methods

A. Frame Selection

To select frame n for spatial-angular compounding, an external tracking system records the US probe pose (T_{Probe}) with each image acquisition, and this pose can be converted to the PA image pose (T_{PA}) through a pre-computed calibration transformation (T_{Cali}) [45], as illustrated in Fig. 1(a). T_{PA} may then be registered to the reference frame (i.e., the first frame) in an acquired image sequence. This relative pose information ($T_{PA,Rel}$) can be used to select in-plane images, and reject out-of-plane images. The relationship between the relative transformations of selected and reference frames is described by the following equations:

$$T_{PA}(n) = T_{Probe}(n) \cdot T_{Cali} \tag{1}$$

$$T_{PA,Rel}(n) = T_{PA}(n)^{-1} \cdot T_{PA,Ref} \tag{2}$$

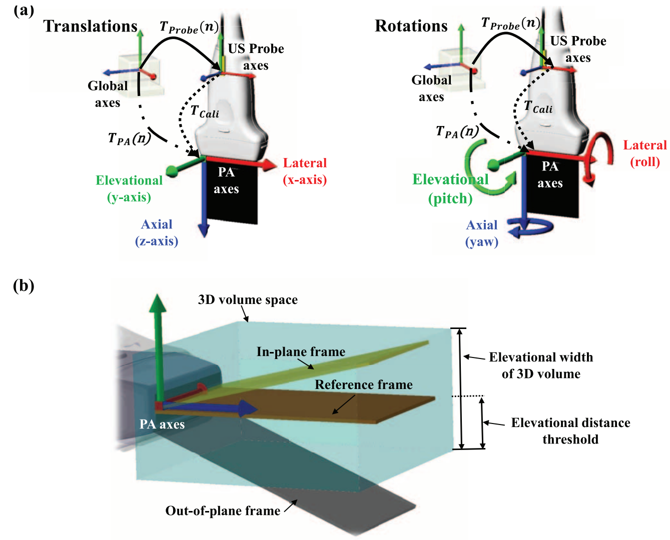

Fig. 1. (a) Coordinate systems of spatially tracked PA images and (b) definitions of in-plane and out-of-plane images based on the user-defined elevational distance thresholds.

where $T_{PA}(n)^{-1}$ is the inverse matrix of the pose of the selected frame and $T_{PA,Ref}$ represents the pose information of the reference frame.

Two threshhold values were considered for the frame selector to ensure that all compounded images are contained within similar planes. Fig. 1(b) illustrates how an in-plane or out-of-plane image was defined with the relative elevational distance threshold. If the maximum elevational distance between a PA frame being considered and the reference image was smaller than this threshold, the frame was sorted as being in-plane, and it was used for the compounding operation. The second threshold value was the relative elevational rotation angle, as the recorded PA signal and noise regions are dependent on both translations and rotations of the ultrasound transducer. Images outside of these two threshold values were considered as out-of-plane images and rejected from the compounding operation.

B. Compounding PA Images

Fig. 2 shows schematic illustrations of compounding with (a) averaging, (b) weighted-averaging, and (c) selective-averaging. These three compounding methods are based on spatial registration of the lateral and axial pixel location of a compounded image with indices i_c and j_c, respectively, defined as:

$$\begin{bmatrix} i_c \\ j_c \\ 0 \\ 1 \end{bmatrix} = \begin{bmatrix} \frac{1}{s_{ic}} & 0 & 0 & 0 \\ 0 & \frac{1}{s_{jc}} & 0 & 0 \\ 0 & 0 & 1 & 0 \\ 0 & 0 & 0 & 1 \end{bmatrix} \cdot \left(T_{PA,Rel}(n)^{-1} \cdot \begin{bmatrix} s_{is}(n) & 0 & 0 & 0 \\ 0 & s_{js}(n) & 0 & 0 \\ 0 & 0 & 1 & 0 \\ 0 & 0 & 0 & 1 \end{bmatrix} \cdot \begin{bmatrix} i_s(n) \\ j_s(n) \\ 0 \\ 1 \end{bmatrix} \right) \tag{3}$$

where $i_s(n)$ and $j_s(n)$ represent the lateral and axial pixel locations, respectively, in one of the selected in-plane images, and $T_{PA,Rel}(n)^{-1}$ is the inverse matrix of the relative transformation of the selected frame. The lateral and axial pixel spacings of

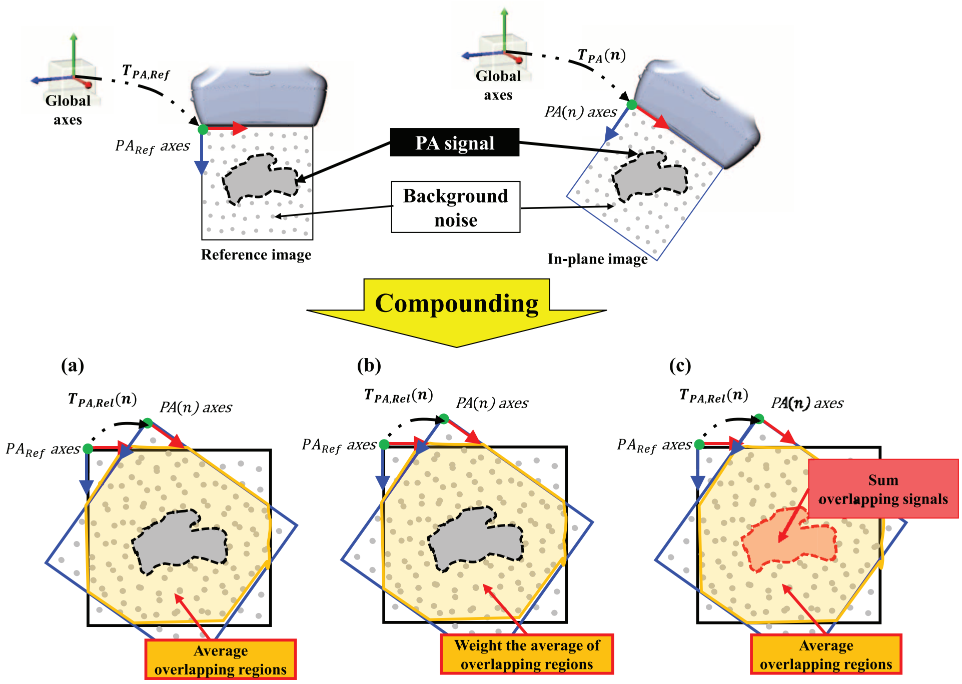

Fig. 2. Schematic illustrations of spatial-angular compounding methods: (a) average, (b) weighted-average and (c) selective-average.

the compounded image are represented by s_{ic} and s_{jc}, respectively, while those of the selected in-plane image are represented by $s_{is}(n)$ and $s_{js}(n)$, respectively. All four pixel spacings have units of mm/pixel.

1) Conventional Compounding: Fig. 2(a) describes the conventional compounding operator, which can be expressed as the following equation:

$$Img_{comp}(i_c, j_c) = \frac{1}{N} Img_{ref}(i_c, j_c) + \frac{1}{N} \sum_{n=2}^{N} Img_{sel}(i_s(n), j_s(n)) \quad (4)$$

where Img_{comp}, Img_{ref} and Img_{sel} are the signal intensities of a compounded image, reference image, and the selected in-plane image, respectively, and N is the total number of compounded images.

Conventional free-hand compounding uses the relative pose information of each PA image and relies on an external tracking system. However, the typical tracking accuracy of optical or EM tracking systems ($0.20 - 0.3$ mm [46]) causes accumulation of errors in the spatial registration between a reference and selected images, and therefore generates distorted PA signals in compounded images [21].

2) Weighted-Average Compounding: To overcome challenges with spatial registration and the resulting signal distortion, we propose weighted-average compounding, as illustrated in Fig. 2(b). The weight factor ($w_{i_c,j_c}(n)$) represents a ratio of normalized difference between signal intensities in a reference frame (Img_{ref}) and a selected PA frame (Img_{sel}):

$$w_{i_c,j_c}(n) = 1 - \left| \frac{Img_{ref}(i_c, j_c) - Img_{sel}(i_s(n), j_s(n))}{\max(Img_{ref}(i_c, j_c), Img_{sel}(i_s(n), j_s(n)))} \right| \quad (5)$$

Note that the weight factor is not constant and can vary with each pixel. This weight factor is high when signals overlap and low when they do not, and it modulates the intensities of signals in the selected image, prior to compounding as described by the following equation:

$$Img_{comp}(i_c, j_c) = \frac{1}{N} Img_{ref}(i_c, j_c) + \frac{1}{N} \sum_{n=2}^{N} \{Img_{sel}(i_s(n), j_s(n)) \cdot w_{i_c,j_c}(n)\} \quad (6)$$

3) Selective-Average Compounding: Selective-average compounding was additionally designed to overcome limitations with the accumulation of tracking errors, particularly when there are large variations in electronic background noise. It identifies and sums overlapping regions of PA signal with higher amplitudes than a pre-defined threshold, as illustrated in Fig. 2(c). The pre-defined threshold value is calculated by an iterative confidence interval of the background noise of PA images. The noise ($\mathcal{N}$) and signal ($\mathcal{S}$) are first sorted by a temporary threshold value ($\mathcal{T}'$) as described by:

$$Img_{sel}(i_s, j_s) \rightarrow \begin{cases} \mathcal{N}(\iota), & \text{if } Img_{sel}(i_s, j_s) \leq \mathcal{T}'(\iota) \\ \mathcal{S}(\iota), & \text{if } Img_{sel}(i_s, j_s) > \mathcal{T}'(\iota) \end{cases} \quad (7)$$

where, ι is the iteration number and $\mathcal{T}'$ represents a temporary threshold. An initial ($\iota = 1$) threshold value $\mathcal{T}'(1)$ is the standard deviation of the PA image data. The updated temporary threshold value $\mathcal{T}'(\iota+1)$ is the Rayleigh inverse cumulative distribution [48] computed with a standard deviation of noise data ($\sigma_{\mathcal{N}(\iota)}$) and a confidence coefficient ($\mathcal{C}$) defined as 0.99999:

$$\mathcal{T}'(\iota + 1) = \sqrt{-2\sigma^2_{\mathcal{N}(\iota)} \cdot \log_{10}(1 - \mathcal{C})} \quad (8)$$

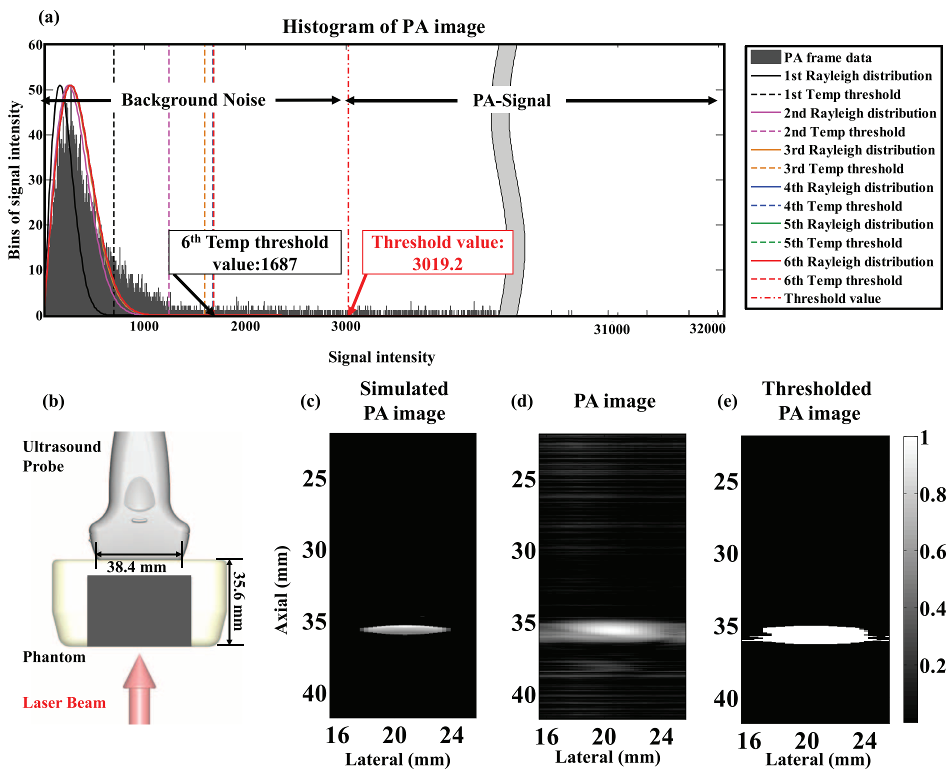

Fig. 3. Results of the user-defined threshold values using an iterative confidence interval of noise for selective-averaging: (a) histogram of values representing the confidence level of noise data (8) and the corresponding Rayleigh distribution of each iteration computation; (b) schematic illustration of the spatial relationships among the phantom, probe, and laser beam and (c) corresponding example of an expected PA image (simulated with the k-Wave toolkit [47]); (d) actual PA image from which the initial histogram in (a) was derived; and (e) corresponding thresholded PA image with the threshold value ($\mathcal{T} = 3019.2$) computed with the (10), where white indicates signal and black indicates noise.

An error threshold ($\mathcal{T}'_{err}(\iota+1)$) is then calculated based on $\mathcal{T}'(\iota+1)$ and $\mathcal{T}'(\iota)$ as described in the following equation:

$$\mathcal{T}'_{err}(\iota+1) = \frac{\mathcal{T}'(\iota+1) - \mathcal{T}'(\iota)}{\mathcal{T}'(\iota)} \tag{9}$$

When $\mathcal{T}'_{err}(\iota+1) \geq 0.0001$, the process ((7)–(9) is repeated with PA data thresholded by $\mathcal{T}'(\iota+1)$. Otherwise, a final threshold value ($\mathcal{T}$) is calculated with the average, $\mathcal{S}_\mu$, and minimum, $\mathcal{S}_{\min}$, values of the signal data as described by:

$$\mathcal{T} = \frac{\mathcal{S}_\mu(\iota+1) - \mathcal{S}_{\min}(\iota+1)}{2} \tag{10}$$

This thresholding iteration process is illustrated in Fig. 3, and it was applied to all selected PA frames. The expected image (Fig. 3(c)) was simulated with the k-Wave toolkit [47], using a 3D fast Fourier transform reconstruction for a planar sensor similar to our probe geometry. The 'makeBall' function was utilized for the initial pressure distribution, assuming a 'ball radius' of 10 grid points, which corresponds to 0.385 mm (axial) $\times$ 3 mm (lateral) $\times$ 2 mm (elevation). The actual distribution depends on the optical absorption profile of the black plastisol material. A compounded image with selective-averaging is computed by summation of the signal intensities of the reference and selected frames as described by:

$$Img_{comp}(i_c, j_c) = Img_{ref}(i_c, j_c) + \sum_{n=2}^{M} Img_{sel}(i_s(n), j_s(n)) \tag{11}$$

where, M represents the number of overlapping signals at the position $Img_{comp}(i_c, j_c)$. The remaining overlapping regions are compounded using (4).

Fig. 4 illustrates the data flowchart for generating reference and compounded PA images. Note that the three compounding operators (average, weighted-average and selective-average) were applied to envelope-detected data and not to pre- or post-beamformed radio frequency (RF) data as in our previous publication [21], because the tracking accuracy is not suitable to account for the phase sensitivity of the RF data.

C. Experimental Procedure

A Q-switched Nd:YAG laser (Quantel, Les Ulis, France) operated at a wavelength of 1064 nm irradiated a plastisol phantom embedded with a black rectangular region to generate PA signals, as illustrated in Fig. 3(b). The laser beam was fixed relative to the phantom. The US equipment consists of a SonixDAQ (Ultrasonix Co., Vancouver, Canada) device, a hand-held L14–5W/38 (Ultrasonix Co., Vancouver, Canada) US probe and Sonix-CEP (Ultrasonix Co., Vancouver, Canada) system. Pose information was recored with a medSAFE (Ascension Technology Co., Milton, USA) EM tracking system. A layer of ultrasound transmission gel was placed between the phantom and hand-held US probe, which was rotated about its elevation axis with minimal rotations about the axial and lateral axes. Transistor-transistor logic (TTL) trigger signals from the laser system were converted to a RS232 protocol with our custom-built controller board, and sent to our *MUSiiC*

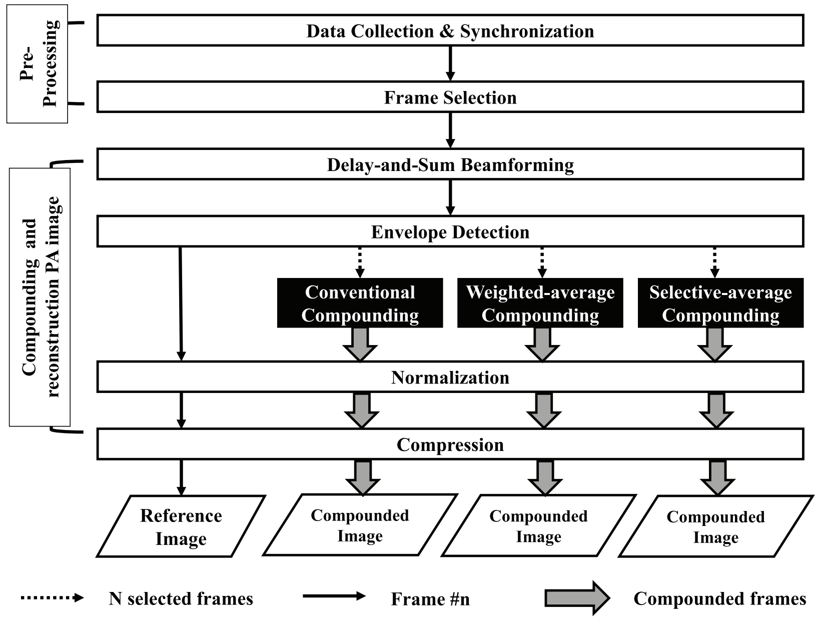

Fig. 4. Flowchart for spatial angular compounding of PA images reconstruction.

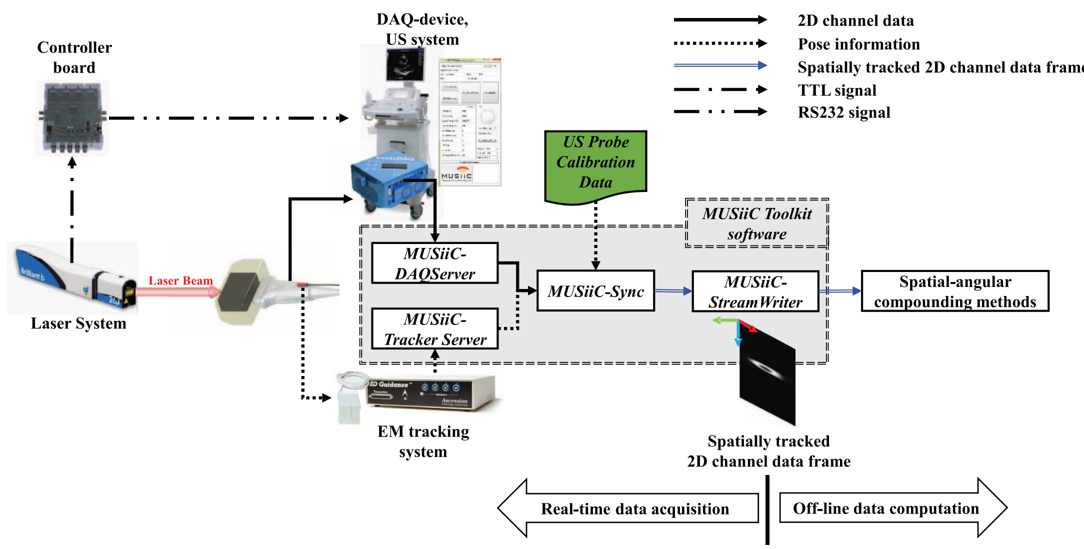

Fig. 5. System components and work-flow for spatial-angular compounding of PA images.

toolkit software, which contains a *MUSiiC-DAQServer* [44] to acquire channel data frames in real-time and measure the data acquisition timestamp of each PA frame, a spatial tracking software module (*MUSiiC-TrackerServer* [44]) to acquire EM tracking information, a *MUSiiC-Sync* software module to synchronize simultaneously acquired 2D PA frame and pose information, and a *MUSiiC-Stream Writer* software module to save spatially-tracked 2D frames to a local hard disk. Spatial-angular compounding methods were then applied off-line. The relationship between the system and software components is illustrated in Fig. 5.

To determine optimal threshold values for frame-selection, the relative elevational distance threshold was varied from 0.5 mm to 2.5 mm in 0.5 mm increments with the relative elevational rotation threshold fixed at values ranging from 0.25° to 7.00° in 0.25° increments.

To determine the noise characteristics of acquired images and their relevance to spatial compounding, a noise region of interest (ROI) in the reference frame was correlated (using normalized cross correlation) with ROIs in the same location of each acquired frame. Results were arranged as a function of elevational distance and rotation relative to the reference.

To evaluate the quality of compounded PA images, contrast, CNR, and SNR were computed with normalized envelope-detected data as follows [8], [14]:

$$\text{Contrast} = \frac{\mu_s - \mu_n}{\mu_n} \tag{12}$$

$$\text{CNR} = \frac{|\mu_s - \mu_n|}{\sigma_n} \tag{13}$$

$$\text{SNR} = \frac{\mu_s}{\sigma_n} \tag{14}$$

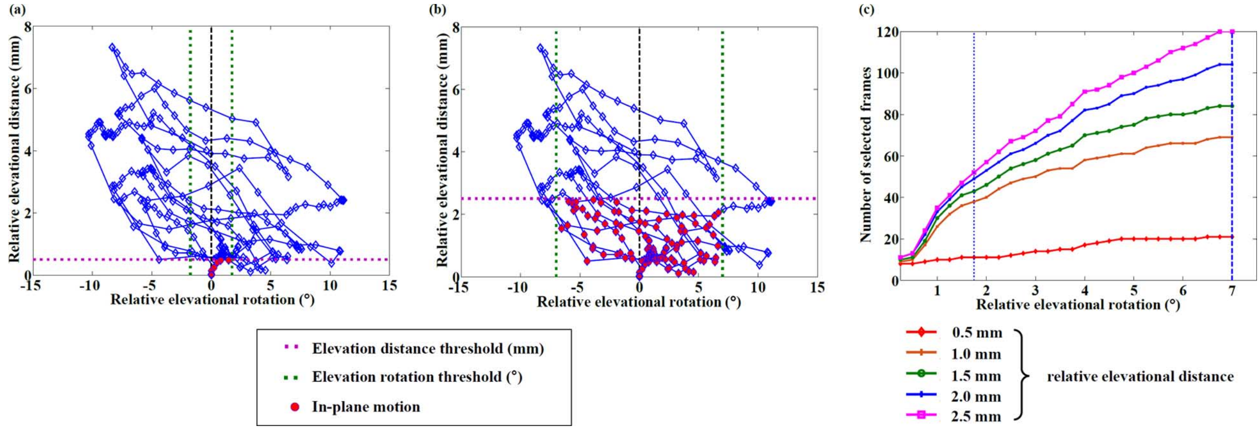

Fig. 6. Selected frames as function of user-defined threshold values: (a) 1.75° relative elevational rotation and 0.5 mm relative elevational distance, and (b) 7.0° relative elevational rotation and 2.5 mm relative elevational distance, where the red dots indicate selected frames given the defined threshold values. (c) The number of selected frames as function of user-defined threshold values, with vertical lines corresponding to the elevational rotation thresholds illustrated in (a) and (b), respectively.

where, μ_s represents the average value of the image intensities in the selected PA signal ROI surrounding the maximum signal intensity and μ_n and σ_n represent the average and standard deviation, respectively, of image intensities in the background noise ROI. The size of the ROIs were fixed to 4.2 mm in the lateral dimension and 1.0 mm in the axial dimension. The noise ROI was located above the signal ROI, and the distance between two ROIs was fixed to 0 mm in the lateral dimension and 7.7 mm in the axial dimension.

In addition, the lateral and axial full width at half maximum (FWHM) of PA signals were measured to determine the similarity of compounded PA signals compared to the reference PA signal. Although the signals were not point targets to provide absolute measurements of resolution [2], we assume that the differences among these measurements provide some indication of corresponding differences in resolution.

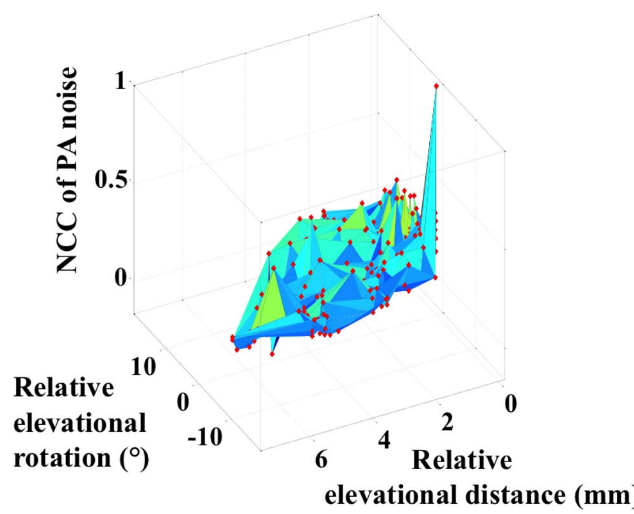

Fig. 7. Surface plot of the normalized cross-correlation (NCC) of PA noise when comparing acquired PA frames with the reference frame, as a function of relative elevational rotation (°) and distance (mm).

III. Results

Figs. 6(a) and 6(b) show the relative elevational pose of the tracked PA images. Each point represents one relative elevational pose and the connector line shows the time trajectory from the reference frame (i.e., the first acquired image). The red points indicate PA frames that were selected based on the user-defined thresholds. In Fig. 6(a), 11 PA frames were selected with relative elevational rotation and elevational distance thresholds of 1.75° and 0.5 mm, respectively. These thresholds represent minimal deviations about the reference image. A total of 120 PA frames were allowed by the frame-selection parameters displayed in Fig. 6(b), where the relative elevational rotation and distance thresholds were 7.0° and 2.5 mm, respectively. Note that increasing the threshold values increase the number of images that are compounded as shown in Fig. 6(c).

Fig. 7 shows a surface plot of the normalized cross-correlation (NCC) values for PA image background noise displayed as a function of the relative pose of the tracked PA images. Each point represents the noise ROI of one PA image correlated with that of the reference PA image. This result demonstrates that PA image background noise rapidly decorrelates with minimal probe perturbation (i.e., translation or rotation). This rapid decorrelation is the reason why multiple PA images may be compounded to improve image quality.

Fig. 8 displays reference and compounded PA images based on the selected frames illustrated in Figs. 6(a) and 6(b). Shifts (i.e., Δx and Δz) between maximum signal intensity in the reference and compounded images are reported below each image defined relative to the axes shown in Fig. 1(a). With small relative motion, the selective-average compounded image has the least signal shift as shown in Fig. 8(b). With large relative motion, weighted-average compounding generated the smallest overall signal shift (Fig. 8(c)). In addition to these signal shifts, the shape and distribution of compounded PA signals were distorted when compared to the reference image, particularly for large relative motion, with the greatest signal preservation obtained with weighted-average compounding.

Fig. 9 shows the image quality metrics of PA images compounded with the three methods. The abscissa of each plot represents relative elevational rotation (°), while the legend indicates the relative elevational distance (mm) for selecting

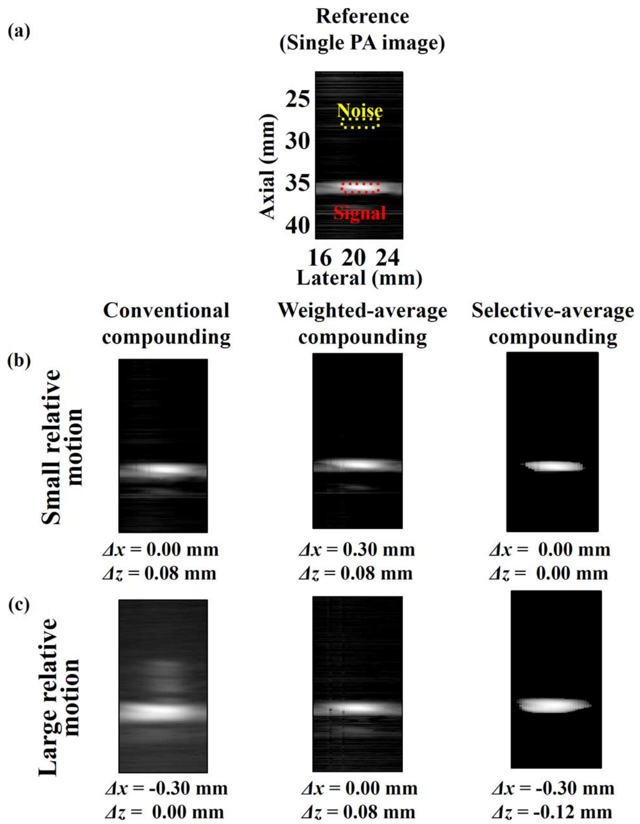

Fig. 8. (a) Single PA reference image and compounded images with (b) relative elevational rotation and relative elevational distance threshold of 1.75° and 0.5 mm, respectively (i.e., small relative motion) and (c) relative elevational rotation and relative elevational distance threshold of 7.0° and 2.5 mm., respectively (i.e., large relative motion). The signal shift $(\Delta x, \Delta z)$ between the reference PA image and compounded PA image are reported below each compounded PA image. Each compounded image is taken from the same axial and lateral distances reported in (a). All images shown with 40 dB dynamic range.

in-plane frames to be compounded. The two vertical lines in each plot indicate 1.75° and 7.00° of relative elevational rotation, which corresponds to the thresholds chosen to display the images in Fig. 8. The solid horizontal lines indicate the mean values of all collected frames with shaded error bars showing $\pm$ one standard deviation. These values for contrast, CNR, SNR, lateral FWHM, and axial FWHM were 14 ± 23, 30 ± 48, 32 ± 48, 3.75 ± 0.35 mm and 0.93 ± 0.94 mm, respectively. Note that each plot is limited to 0, so negative values are not displayed. Compounded PA images with weighted-averaging (second column of Fig. 9) had a up to 1.47 times higher contrast compared to conventional compounded PA images (first column of Fig. 9). However, the conventional compounded PA images had up 5 times higher CNR and SNR compared to the weighted-average compounded PA images.

Contrast decreased over the first few elevational rotations $(0.75^{\circ} - 1.25^{\circ})$ with the larger relative elevational distances $(1.0 \text{ mm} - 2.5 \text{ mm})$, likely because of the registration errors or the increased misalignment between the laser and probe, indicating the importance of frame-selection for average and weighted-average compounding. This dependence is removed with selective-averaging.

Compounding with selective-averaging generated images with up to 181, 1665 and 1568 times higher contrast, CNR and SNR, respectively, than the corresponding mean values of all collected PA frames. This method produced the best contrast, CNR and SNR when compared to images compounded with averaging and weighted-averaging. Contrast increases with the number of larger threshold values for the selective averaging method because more frames are included with this increase in relative elevational rotation and/or distance. The signal region is summed (as shown in Fig. 2) while the background region is averaged. Increasing the number of frames inherently increases the value of the summed signal. Fluctuations are present because the number of frames does not consistently increase with an increase in relative elevational rotation and/or distance as shown in Fig. 6(c).

The lateral and axial FWHM (Figs. 9(d) and 9(e), respectively) of conventional compounded PA signals generally increased as the relative elevational rotation and distance increased. This increase indicates signal blurring and loss of resolution. Unlike compounding with conventional averaging, the lateral and axial FWHM were mostly within one standard deviation of all acquired frames when compounding with weighted- and selective-averaging.

Fig. 10 shows the image quality of compounded PA images as a function of the number of selected frames for all previously reported thresholds. The measured values for average and weighted-average compounding are associated with the left ordinate, while the right ordinate represents the values for selective-average compounding. The solid horizontal lines in each plot represent the mean values of all collected frames with shaded error bars spanning $\pm$ one standard deviation (values are associated with left ordinate).

The image quality of compounded PA images with selective-averaging was highly dependent on the number of selected frames. In particular, contrast, CNR, and SNR ranged $323 - 2622$, $1188 - 50494$ and $1191 - 50513$, respectively, as the number of selected frames increased. Compounding with averaging and weighted-averaging produced higher contrast when the number of frames was ≤ 24 (i.e., 2.5 mm and 0.75° elevational distance and rotation thresholds, respectively), with minimal change in contrast when more frames were included. The CNR and SNR generally increased with the number of frames for compounding with conventional and selective averaging, while they were relatively constant when compounding with weighted averaging.

The lateral FWHM (Fig. 10(d)) of images compounded with conventional averaging and selective-averaging linearly increased when the number of frames was $\geq$ 32 (i.e., 1.0 mm and 1.25 ° elevational distance and rotation thresholds, respectively), indicating lateral resolution degradation, with minimal change observed for weighted-averaging over this range. Nonetheless, note that conventional averaging causes the largest degradation of lateral resolution as the number of frames increases.

The axial FWHM (Fig. 10(e)) of images compounded with conventional and selective-averaging increased and then remained relatively constant as the number of frames increased, while that of weighted-averaging remained relatively constant for the majority of compounded images. Despite these trends for axial FWHM, all frames are within one standard deviation of the mean of all collected frames.

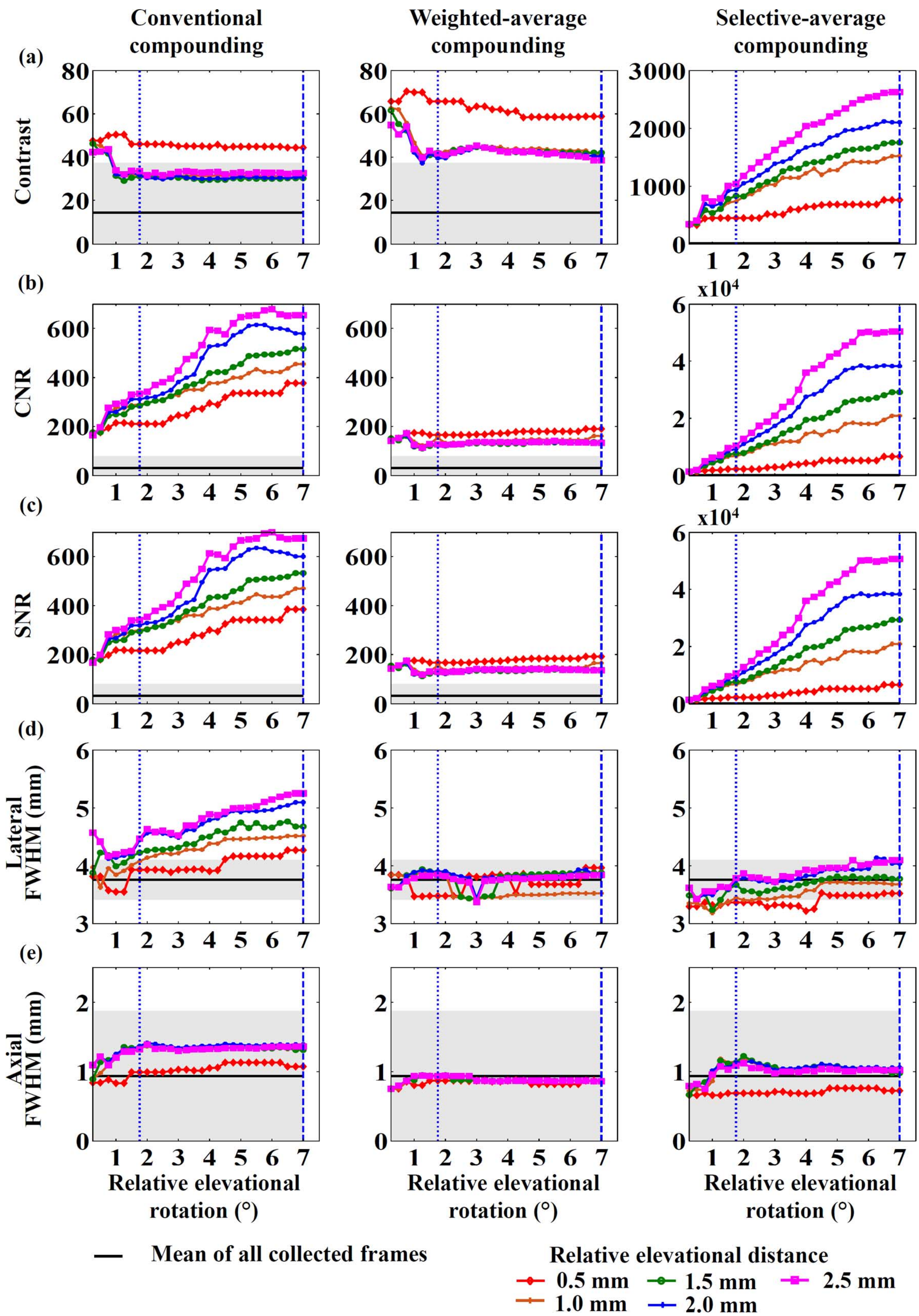

Fig. 9. Image quality metrics: (a) CNR, (b) SNR (c) Contrast (d) lateral FWHM and (e) axial FWHM as a function of the relative elevational rotation threshold for each relative elevational distance threshold shown in the legend. Each column shows results for one of the three compounding methods: conventional averaging (left), weighted averaging (middle) and selective averaging (right). The mean value of all collected frames is represented by the black line. The gray shading represents data that are within one standard deviation of the mean (negative values are not shown). The two vertical lines in each plot correspond to the values for the two relative elevational rotation thresholds shown in Fig. 8: small (left) and large (right).

IV. Discussion

We investigated three compounding methods that require spatial tracking of free-hand PA images to improve image quality. Contrary to US imaging, where the success of spatial compounding relies on the combination of fully decorrelated speckle patterns, which can be achieved with large relative

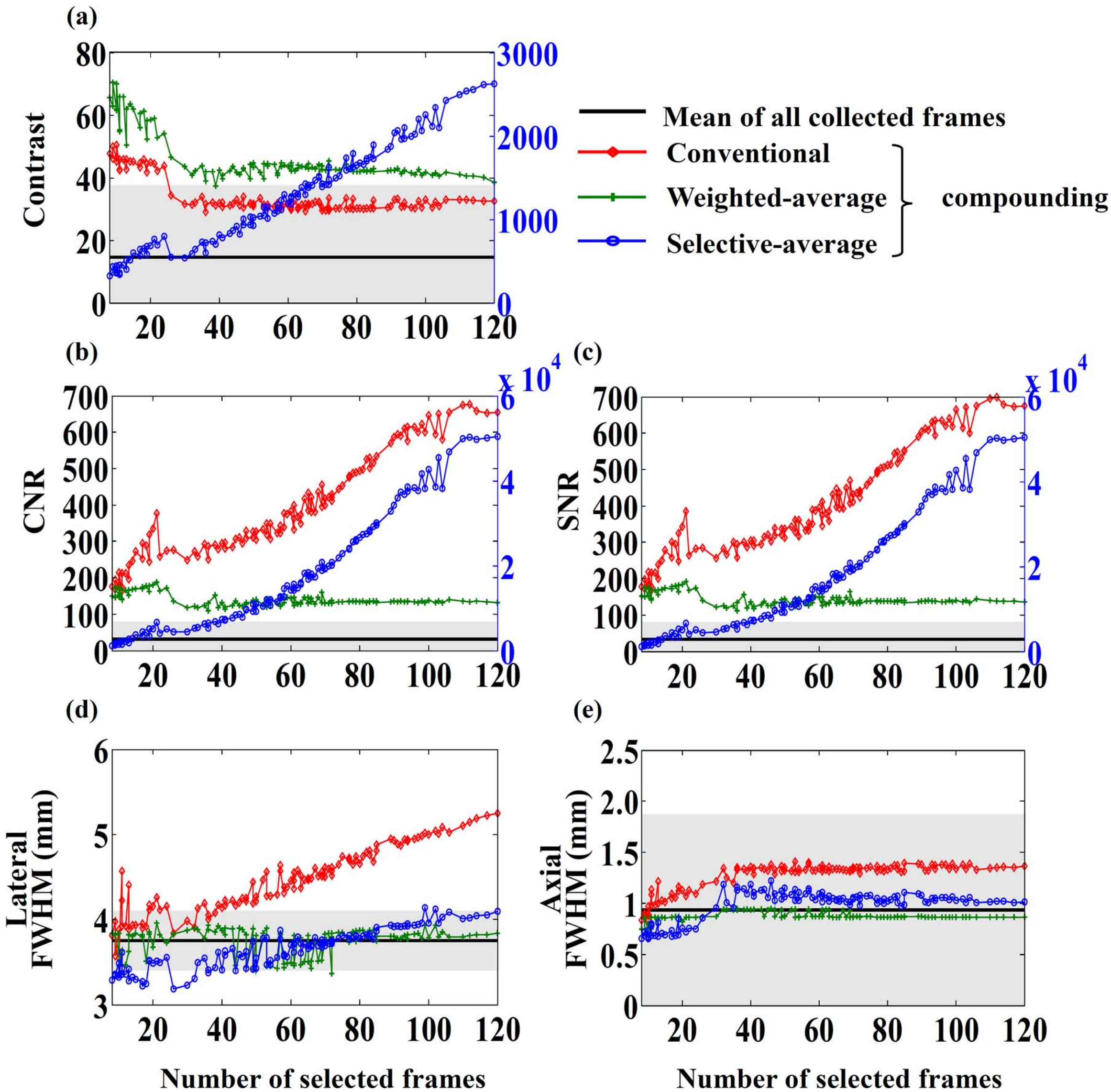

Fig. 10. (a) CNR, (b) SNR (c) Contrast (d) lateral FWHM, and (e) axial FWHM of compounded PA images as a function of the number of selected frames for the three compounding operators shown in the legend. The mean value is the black line. The gray shading represents data that are within one standard deviation of the mean (negative values are not shown). The values for selective-average compounding correspond with the right ordinate, all other values correspond with the left ordinate.

translations [10] or rotations [41], the background noise of PA images rapidly decorrelates (e.g., NCC < 0.5), with minimal perturbation from an initial probe position, as shown in Fig. 7, whereas ultrasound speckle correlation is greater than 0.9 for similar values of probe perturbation [10], [49]. Thus improved contrast, CNR, and SNR were achieved with as little as 0.5 mm and 0.75° frame separation, as shown in Fig. 9 and in our previous publication [21]. In addition, Fig. 7 supports the work of Forbrich *et al.* [50] who used a form of spatial angular compounding for photoacoustic microscopy to visualize excised kidneys and hindlimb mouse tumors.

Compounding with conventional averaging is straightforward and relies solely on the tracking information. The main limitation with this method is signal blurring caused by the accumulation of tracking errors with large free hand motion as shown in Fig. 8 and quantified with the lateral FWHM measurements in Fig. 9(d). Thus, this method is most useful when probe motion is restricted to minimal translational and rotational perturbations, which is possible with robotic assistance or electronic beam steering implemented with a relatively stationary probe. The method is also more advantageous when structures are larger than the comparative loss in resolution relative to the mean (i.e., up to 1.5 mm, depending on the frame selection parameters).

Compounding with weighted- and selective-averaging utilizes tracking information along with the intensity values in each image to overcome limitations with tracking accuracy and provide improved quality when PA signals have significant overlap. Weighted-average compounding considers the error in spatial registration by providing a high weighting when there is signal overlap and a lower weighting when there is a mismatch due to registration errors. Consequently, the image quality of weighted-average compounded images were less sensitive to the elevational rotation thresholds as shown in Figs. 9(a)–9(c). In addition, as a result of the weighting factor, this method generated compounded PA signals that were similar in size to the reference PA signal and insensitive to large motion, with CNR and SNR values that were independent of the number of frames, unlike PA signals compounded with averaging and selective-averaging (Figs. 10(d) and 10(e)).

The CNR and SNR of images compounded with weighted-averaging are lower compared to those of the other two compounding methods because the weighting factor (applied to overcome frame misalignment caused by tracking or quantization errors) reduces overall signal magnitudes. The lack of an increase in contrast, CNR, or SNR as a function of the number of frames for weighted-average compounding occurs because of the higher standard deviation of the background noise likely caused by the pixel-by-pixel variation of the weight factor ((5)). This increase (which is not observed for the other two compounding methods) results in either reduced or similar contrast, CNR, and SNR when compared to a minimal number of compounded frames (see Fig. 10). Nonetheless, the contrast, CNR, and SNR of these images compounded with weighted averaging are still considered improved when compared to the mean $\pm$ one standard deviation of all 120 individual image frames (black line $\pm$ shaded area).

Selective-averaging provides orders of magnitude higher contrast, CNR, and SNR because the intensity ratio between compounded signals and noise is increased by a multiple of the number of compounded frames (particularly when compared to conventional compounding). This increased contrast, CNR, and SNR is expected when considering that this method sums regions of overlapping signals and averages all other data, hence the difference between the amplitude of PA signal and noise regions increases with the number of compounded frames. As selective-averaging depends on the separation of signal and noise, resolution could be improved with alternative separation methods (e.g., Otsu method [51], balanced histogram thresholding [52]), although the method herein might be sufficient as it provides a resolution within one standard deviation of the mean of all selected frames. PA images compounded with selective-averaging are favorable given the significantly higher contrast, CNR, and SNR for small and large relative motions. The performance increase with more frames makes it particularly advantageous for lasers with low energies and high pulse repetition frequencies (e.g., pulsed laser diodes).

Examples of potential applications for selective- and weighted-averaging (which are most useful when the noise appears in a different location with each viewing angle) include removing reverberation clutter caused by closely spaced hyperechoic implants (e.g., brachytheraphy seeds [9]) or acoustically heterogenous anatomical structures (e.g., bone or lungs [53]), removing diffuse clutter while maintaining diffuse signals in molecular imaging, and rotating around entire objects to acquire images as in breast or small animal imaging. We expect that the presented compounding methods can be implemented in real-time with the parallel computation capability of graphics processing units (GPUs) [54]. These and related applications will be the focus of our future investigations, which will implement the novel hardware and software system components presented herein to accomplish an array of imaging tasks, including testing with more complicated phantoms, animal models, and humans.

V. Conclusion

We demonstrated spatial-angular compounding of PA images using conventional, weighted, and selective averaging with a fixed light source and a freehand probe. An experimental study of these three compounding methods revealed improved contrast, CNR, and SNR with each method compared to the corresponding mean values of individual images. Average compounding enhanced PA images with minimal relative motion required to preserve the size of signals. Both weighted- and selective-averaging produced signal sizes that were within one standard deviation of all PA signals acquired, yet those of weighted-averaging were most similar to the mean of all frames. In addition, weighted-averaging was the least sensitive to large motions and the number of selected frames, while selective-averaging offered the greatest improvements in contrast, CNR, and SNR. These three compounding methods have unique clinical advantages and promise to enhance PA images in photoacoustic imaging applications that range from detecting breast cancer to localizing metal implants and removing clutter from molecular, pre-clinical, and clinical images.

References

[1] X. Wang, J. B. Fowlkes, J. M. Cannata, C. Hu, and P. L. Carson, "Photoacoustic imaging with a commercial ultrasound system and a custom probe," *Ultrasound Med. Biol.* vol. 37, no. 3, pp. 484–492, 2011 [Online]. Available: http://www.sciencedirect.com/science/article/pii/S030156291000668X

[2] M. Xu and L. V. Wang, "Photoacoustic imaging in biomedicine," *Rev. Sci. Instrum.*, vol. 77, no. 4, p. 041101, 2006.

[3] H. J. Kang *et al.*, "Software framework of a real-time pre-beamformed RF data acquisition of an ultrasound research scanner," *SPIE Med. Imag.*, p. 83201F, 2012.

[4] M. Heijblom *et al.*, "Visualizing breast cancer using the twente photoacoustic mammoscope: What do we learn from twelve new patient measurements?," *Opt. Exp.* vol. 20, no. 11, pp. 11582–11597, May 2012 [Online]. Available: http://www.opticsexpress.org/abstract.cfm?URI=oe-20-11-11582

[5] S. Sethuraman, J. H. Amirian, S. H. Litovsky, R. W. Smalling, and S. Y. Emelianov, "Spectroscopic intravascular photoacoustic imaging to differentiate atherosclerotic plaques," *Opt. Exp.*, vol. 16, no. 5, pp. 3362–3367, 2008.

[6] J. Shah *et al.*, "Photoacoustic imaging and temperature measurement for photothermal cancer therapy," *J. Biomed. Opt.*, vol. 13, no. 3, p. 034024, 2008.

[7] N. Kuo, H. J. Kang, T. DeJournett, J. Spicer, and E. Boctor, "Photoacoustic imaging of prostate brachytherapy seeds in ex vivo prostate," *SPIE Med. Imag.*, p. 796409, 2011.

[8] J. L. Su, R. R. Bouchard, A. B. Karpiouk, J. D. Hazle, and S. Y. Emelianov, "Photoacoustic imaging of prostate brachytherapy seeds," *Biomed. Opt. Exp.*, vol. 2, no. 8, pp. 2243–2254, 2011.

[9] M. A. Lediju Bell, N. P. Kuo, D. Y. Song, J. U. Kang, and E. M. Boctor, "In vivo visualization of prostate brachytherapy seeds with photoacoustic imaging," *J. Biomed. Opt.*, vol. 19, no. 12, p. 126011, 2014.

[10] G. Trahey, S. Smith, and O. von Ramm, "Speckle reduction in medical ultrasound via spatial compounding," in *Appl. Optical Instrum. Med. XIV Picture Archiv. Commun. Syst. (PACS IV) Med. Appl. Int. Soc. Opt. Photon.*, 1986, pp. 290–300.

[11] T. Udomchai, Q. Chen, T. Varghese, J. A. Zagzebski, and E. L. Madsen, "Noise reduction using spatial-angular compounding for elastography," *IEEE Trans. Ultrason., Ferroelectr. Freq. Control*, vol. 51, no. 5, pp. 510–520, May 2004.

[12] M. A. Lediju, M. J. Pihl, J. J. Dahl, and G. E. Trahey, "Quantitative assessment of the magnitude, impact and spatial extent of ultrasonic clutter," *Ultrason. Imag.*, vol. 30, no. 3, pp. 151–168, 2008.

[13] B. Pourebrahimi, S. Yoon, D. Dopsa, and M. C. Kolios, "Improving the quality of photoacoustic images using the short-lag spatial coherence imaging technique," *SPIE BiOS.*, p. 85813Y, 2013.

[14] M. A. Lediju Bell, N. Kuo, D. Y. Song, and E. M. Boctor, "Short-lag spatial coherence beamforming of photoacoustic images for enhanced visualization of prostate brachytherapy seeds," *Biomed. Opt. Exp.*, vol. 4, no. 10, pp. 1964–1977, 2013.

[15] M. Jaeger, D. Harris-Birtill, A. Gertsch, E. OÕFlynn, and J. Bamber, "Deformation-compensated averaging for clutter reduction in epiphotoacoustic imaging in vivo," *J. ofBiomed. Opt.*, vol. 17, no. 6, pp. 0660071–0660078, 2012.
[16] T. J. Allen and P. C. Beard, "Dual wavelength laser diode excitation source for 2d photoacoustic imaging," in *BiOS*, 2007, p. 64371U.
[17] M. A. Lediju Bell, X. Guo, H. J. Kang, and E. Boctor, "Improved contrast in laser-diode-based photoacoustic images with short-lag spatial coherence beamforming," in *Proc. IEEE Ultrason. Symp.*, 2014, pp. 37–40.
[18] S. A. Telenkov, R. Alwi, and A. Mandelis, "Photoacoustic correlation signal-to-noise ratio enhancement by coherent averaging and optical waveform optimization," *Rev. Sci. Instrum.*, vol. 84, no. 10, p. 104907, 2013.
[19] V. Behar, D. Adam, and Z. Friedman, "A new method of spatial compounding imaging," *Ultrasonics*, vol. 41, no. 5, pp. 377–384, 2003.
[20] P.-C. Li and M. O'Donnell, "Elevational spatial compounding," *Ultrason. Imag.*, vol. 16, no. 3, pp. 176–189, 1994.
[21] H. J. Kang, M. A. Lediju Bell, X. Guo, R. H. Taylor, and E. M. Boctor, "Freehand spatial-angular compounding of photoacoustic images," *SPIE BiOS*, p. 894361, 2014.
[22] B. M. Asl and A. Mahloojifar, "Minimum variance beamforming combined with adaptive coherence weighting applied to medical ultrasound imaging," *IEEE Trans. Ultrason., Ferroelectr. Freq. Control*, vol. 56, no. 9, pp. 1923–1931, Sep. 2009.
[23] S. Park, A. B. Karpiouk, S. R. Aglyamov, and S. Y. Emelianov, "Adaptive beamforming for photoacoustic imaging," *Opt. Lett.*, vol. 33, no. 12, pp. 1291–1293, 2008.
[24] Y.-H. Wang and P.-C. Li, "SNR-dependent coherence-based adaptive imaging for high-frame-rate ultrasonic and photoacoustic imaging," *IEEE Trans. Ultrason., Ferroelectr., Freq. Control*, vol. 61, no. 8, pp. 1419–1432, Aug. 2014.
[25] M. Jaeger, J. C. Bamber, and M. Frenz, "Clutter elimination for deep clinical optoacoustic imaging using localised vibration tagging (LOVIT)," *Photoacoustics*, vol. 1, no. 2, pp. 19–29, 2013.
[26] M. A. Lediju *et al.*, "A motion-based approach to abdominal clutter reduction," *IEEE Trans. Ultrason., Ferroelectr. Freq. Control*, vol. 56, no. 11, pp. 2437–2449, Nov. 2009.
[27] M. A. Lediju, G. E. Trahey, B. C. Byram, and J. J. Dahl, "Short-lag spatial coherence of backscattered echoes: Imaging characteristics," *IEEE Trans. Ultrason., Ferroelectr. Freq. Control*, vol. 58, no. 7, pp. 1377–1388, Jul. 2011.
[28] J. J. Dahl, D. Hyun, M. Lediju, and G. E. Trahey, "Lesion detectability in diagnostic ultrasound with short-lag spatial coherence imaging," *Ultrason. Imag.*, vol. 33, no. 2, pp. 119–133, 2011.
[29] M. A. Lediju Bell, A. K. Ostrowski, K. Li, P. Kazanzides, and E. M. Boctor, "Localization of transcranial targets for photoacoustic-guided endonasal surgeries," *Photoacoustics*, vol. 3, no. 2, pp. 78–87, 2015.
[30] E. J. Alles, M. Jaeger, and J. C. Bamber, "Photoacoustic clutter reduction using short-lag spatial coherence weighted imaging," in *Proc. IEEE Int. Ultrason. Symp.*, Sep. 2014, pp. 41–44.
[31] M. A. Lediju Bell, X. Guo, D. Y. Song, and E. M. Boctor, "Transurethral light delivery for prostate photoacoustic imaging," *J. Biomed. Opt.*, vol. 20, no. 3, p. 036002, 2015.
[32] L. Pan *et al.*, "Improving photoacoustic imaging contrast of brachytherapy seeds," *SPIE BiOS*, pp. 85814B–85814B, 2013.
[33] T. Mitcham *et al.*, "Modulation of photoacoustic signal generation from metallic surfaces," *J. Biomed. Opt.*, vol. 18, no. 5, p. 056008, 2013.
[34] J. F. Krücker, C. R. Meyer, G. L. LeCarpentier, J. B. Fowlkes, and P. L. Carson, "3d spatial compounding of ultrasound images using image-based nonrigid registration," *Ultrasound Med. Biol.*, vol. 26, no. 9, pp. 1475–1488, 2000.
[35] R. Rohling, A. Gee, and L. Berman, "Three-dimensional spatial compounding of ultrasound images," *Med. Image Anal.*, vol. 1, no. 3, pp. 177–193, 1997.
[36] R. R. Entrekin *et al.*, "Real-time spatial compound imaging: Application to breast, vascular, and musculoskeletal ultrasound," *Sem. Ultrasound, CT MRI*, vol. 22, no. 1, pp. 50–64, 2001.
[37] A. L. Gerig, T. Varghese, and J. A. Zagzebski, "Improved parametric imaging of scatterer size estimates using angular compounding," *IEEE Trans Ultrason., Ferroelectr. Freq. Control*, vol. 51, no. 6, pp. 708–715, Jun. 2004.
[38] H. Tu *et al.*, "Optimization of angular and frequency compounding in ultrasonic attenuation estimations," *J. Acoust. Soc. Am.*, vol. 117, no. 5, pp. 3307–3318, 2005.
[39] M. Rao, Q. Chen, H. Shi, and T. Varghese, "Spatial-angular compounding for elastography using beam steering on linear array transducers," *Med. Phys.*, vol. 33, no. 3, pp. 618–626, 2006.
[40] H. H. Hansen, R. G. Lopata, and C. L. de Korte, "Noninvasive carotid strain imaging using angular compounding at large beam steered angles: validation in vessel phantoms," *IEEE Trans. Med. Imag.*, vol. 28, no. 6, pp. 872–880, Jun. 2009.
[41] M. H. Choi and M. H. Bae, "Spatial compounding of ultrasonic diagnostic images for rotating linear probe with geometric parameter error compensation," *J. Elect. Eng. Technol.*, vol. 9, no. 4, pp. 1418–1425, 2014.
[42] G. Trahey, J. Allison, S. Smith, and O. Von Ramm, "A quantitative approach to speckle reduction via frequency compounding," *Ultrason. Imag.*, vol. 8, no. 3, pp. 151–164, 1986.
[43] M. Berson, A. Roncin, and L. Pourcelot, "Compound scanning with an electrically steered beam," *Ultrason. Imag.*, vol. 3, no. 3, pp. 303–308, 1981.
[44] H. J. Kang, X. Guo, R. Z. Azar, A. Cheng, and E. M. Boctor, "Software framework for spatially tracked pre-beamformed RF data acquisition with a freehand clinical ultrasound transducer," *SPIE Med. Imag.*, p. 90401W, 2014.
[45] Z. Yaniv, P. Foroughi, H.-J. Kang, and E. Boctor, "Ultrasound calibration framework for the image-guided surgery toolkit (IGSTK)," *SPIE Med. Imag.*, p. 79641N, 2011.
[46] T. Koivukangas, J. Katisko, and J. Koivukangas, "Technical accuracy of optical and the electromagnetic tracking systems," *Springer Plus* vol. 2, no. 1, 2013 [Online]. Available: http://dx.doi.org/10.1186/2193-1801-2-90
[47] B. E. Treeby and B. T. Cox, "K-wave: Matlab toolbox for the simulation and reconstruction of photoacoustic wave fields," *J. Biomed. Opt.*, vol. 15, no. 2, p. 021314, 2010.
[48] M. Siddiqui, "Statistical inference for rayleigh distributions," *J. Res. Nat. Bureau Standards, Sec. D*, vol. 68, 1964.
[49] M. Rao and T. Varghese, "Correlation analysis for angular compounding in strain imaging," *IEEE Trans. Ultrason., Ferroelectr., Freq. Control*, vol. 54, no. 9, pp. 1903–1907, Sep. 2007.
[50] A. Forbrich, A. Heinmiller, J. Jose, A. Needles, and D. Hirson, "Photoacoustic imaging with rotational compounding for improved signal detection," *SPIE BiOS*, p. 932330, 2015.
[51] N. Otsu, "A threshold selection method from gray-level histograms," *Automatica*, vol. 11, no. 285-296, pp. 23–27, 1975.
[52] A. dos Anjos and H. Shahbazkia, "Bi-level image thresholding—A fast method," *BIOSIGNALS (2)*, pp. 70–76, 2008.
[53] X. L. Dean-Ben, R. Ma, D. Razansky, and V. Ntziachristos, "Statistical approach for optoacoustic image reconstruction in the presence of strong acoustic heterogeneities," *IEEE Trans. Med. Imag.*, vol. 30, no. 2, pp. 401–408, Feb. 2011.
[54] X. L. Dean-Ben, A. Ozbek, and D. Razansky, "Volumetric real-time tracking of peripheral human vasculature with GPU-accelerated three-dimensional optoacoustic tomography," *IEEE Trans. Med. Imag.*, vol. 32, no. 11, pp. 2050–2055, Nov. 2013.